Regular Article - Experimental Physics

Multipole analysis of IceCube data to search for dark matter accumulated in the Galactic halo

IceCube Collaboration

M. G. Aartsen[2], M. Ackermann[45], J. Adams[15], J. A. Aguilar[23], M. Ahlers[28], M. Ahrens[36], D. Altmann[22], T. Anderson[42], C. Arguelles[28], T. C. Arlen[42], J. Auffenberg[1], X. Bai[34], S. W. Barwick[25], V. Baum[29], J. J. Beatty[17,18], J. Becker Tjus[10], K.-H. Becker[44], S. BenZvi[28], P. Berghaus[45], D. Berley[16], E. Bernardini[45], A. Bernhard[31], D. Z. Besson[26], G. Binder[7,8], D. Bindig[44], M. Bissok[1], E. Blaufuss[16], J. Blumenthal[1], D. J. Boersma[43], C. Bohm[36], F. Bos[10], D. Bose[38], S. Böser[11], O. Botner[43], L. Brayeur[13], H.-P. Bretz[45], A. M. Brown[15], J. Casey[5], M. Casier[13], D. Chirkin[28], A. Christov[23], B. Christy[16], K. Clark[39], L. Classen[22], F. Clevermann[20], S. Coenders[31], D. F. Cowen[41,42], A. H. Cruz Silva[45], M. Danninger[36], J. Daughhetee[5], J. C. Davis[17], M. Day[28], J. P. A. M. de André[42], C. De Clercq[13], S. De Ridder[24], P. Desiati[28], K. D. de Vries[13], M. de With[9], T. DeYoung[42], J. C. Díaz-Vélez[28], M. Dunkman[42], R. Eagan[42], B. Eberhardt[29], B. Eichmann[10], J. Eisch[28], S. Euler[43], P. A. Evenson[32], O. Fadiran[28], A. R. Fazely[6], A. Fedynitch[10], J. Feintzeig[28], J. Felde[16], T. Feusels[24], K. Filimonov[7], C. Finley[36], T. Fischer-Wasels[44], S. Flis[36], A. Franckowiak[11], K. Frantzen[20], T. Fuchs[20], T. K. Gaisser[32], J. Gallagher[27], L. Gerhardt[7,8], D. Gier[1], L. Gladstone[28], T. Glüsenkamp[45], A. Goldschmidt[8], G. Golup[13], J. G. Gonzalez[32], J. A. Goodman[16], D. Góra[45], D. T. Grandmont[21], D. Grant[21], P. Gretskov[1], J. C. Groh[42], A. Groß[31], C. Ha[7,8], C. Haack[1], A. Haj Ismail[24], P. Hallen[1], A. Hallgren[43], F. Halzen[28], K. Hanson[12], D. Hebecker[11], D. Heereman[12], D. Heinen[1], K. Helbing[44], R. Hellauer[16], D. Hellwig[1], S. Hickford[15], G. C. Hill[2], K. D. Hoffman[16], R. Hoffmann[44], A. Homeier[11], K. Hoshina[28,b], F. Huang[42], W. Huelsnitz[16], P. O. Hulth[36], K. Hultqvist[36], S. Hussain[32], A. Ishihara[14], E. Jacobi[45], J. Jacobsen[28], K. Jagielski[1], G. S. Japaridze[4], K. Jero[28], O. Jlelati[24], M. Jurkovic[31], B. Kaminsky[45], A. Kappes[22], T. Karg[45], A. Karle[28], M. Kauer[28], J. L. Kelley[28], A. Kheirandish[28], J. Kiryluk[37], J. Kläs[44], S. R. Klein[7,8], J.-H. Köhne[20], G. Kohnen[30], H. Kolanoski[9], A. Koob[1], L. Köpke[29], C. Kopper[28], S. Kopper[44], D. J. Koskinen[19], M. Kowalski[11], A. Kriesten[1], K. Krings[1], G. Kroll[29], M. Kroll[10], J. Kunnen[13], N. Kurahashi[28], T. Kuwabara[32], M. Labare[24], D. T. Larsen[28], M. J. Larson[19], M. Lesiak-Bzdak[37], M. Leuermann[1], J. Leute[31], J. Lünemann[29], O. Macías[15], J. Madsen[35], G. Maggi[13], R. Maruyama[28], K. Mase[14], H. S. Matis[8], F. McNally[28], K. Meagher[16], M. Medici[19], A. Meli[24], T. Meures[12], S. Miarecki[7,8], E. Middell[45], E. Middlemas[28], N. Milke[20], J. Miller[13], L. Mohrmann[45], T. Montaruli[23], R. Morse[28], R. Nahnhauer[45], U. Naumann[44], H. Niederhausen[37], S. C. Nowicki[21], D. R. Nygren[8], A. Obertacke[44], S. Odrowski[21], A. Olivas[16], A. Omairat[44], A. O'Murchadha[12], T. Palczewski[40], L. Paul[1], Ö. Penek[1], J. A. Pepper[40], C. Pérez de los Heros[43], C. Pfendner[17], D. Pieloth[20], E. Pinat[12], J. Posselt[44], P. B. Price[7], G. T. Przybylski[8], J. Pütz[1], M. Quinnan[42], L. Rädel[1], M. Rameez[23], K. Rawlins[3], P. Redl[16], I. Rees[28], R. Reimann[1,a], E. Resconi[31], W. Rhode[20], M. Richman[16], B. Riedel[28], S. Robertson[2], J. P. Rodrigues[28], M. Rongen[1], C. Rott[38], T. Ruhe[20], B. Ruzybayev[32], D. Ryckbosch[24], S. M. Saba[10], H.-G. Sander[29], J. Sandroos[19], M. Santander[28], S. Sarkar[19,33], K. Schatto[29], F. Scheriau[20], T. Schmidt[16], M. Schmitz[20], S. Schoenen[1], S. Schöneberg[10], A. Schönwald[45], A. Schukraft[1], L. Schulte[11], O. Schulz[31], D. Seckel[32], Y. Sestayo[31], S. Seunarine[35], R. Shanidze[45], C. Sheremata[21], M. W. E. Smith[42], D. Soldin[44], G. M. Spiczak[35], C. Spiering[45], M. Stamatikos[17,c], T. Stanev[32], N. A. Stanisha[42], A. Stasik[11], T. Stezelberger[8], R. G. Stokstad[8], A. Stößl[45], E. A. Strahler[13], R. Ström[43], N. L. Strotjohann[11], G. W. Sullivan[16], H. Taavola[43], I. Taboada[5], A. Tamburro[32], A. Tepe[44], S. Ter-Antonyan[6], A. Terliuk[45], G. Tešić[42], S. Tilav[32], P. A. Toale[40], M. N. Tobin[28], D. Tosi[28], M. Tselengidou[22], E. Unger[10], M. Usner[11], S. Vallecorsa[23], N. van Eijndhoven[13], J. Vandenbroucke[28], J. van Santen[28], M. Vehring[1], M. Voge[11], M. Vraeghe[24], C. Walck[36], M. Wallraff[1], Ch. Weaver[28], M. Wellons[28], C. Wendt[28], S. Westerhoff[28], B. J. Whelan[2], N. Whitehorn[28], C. Wichary[1], K. Wiebe[29], C. H. Wiebusch[1], D. R. Williams[40], H. Wissing[16], M. Wolf[36], T. R. Wood[21], K. Woschnagg[7], D. L. Xu[40], X. W. Xu[6], J. P. Yanez[45], G. Yodh[25], S. Yoshida[14], P. Zarzhitsky[40], J. Ziemann[20], S. Zierke[1], M. Zoll[36]

[1] III. Physikalisches Institut, RWTH Aachen University, 52056 Aachen, Germany
[2] School of Chemistry and Physics, University of Adelaide, Adelaide, SA 5005, Australia

[3] Department of Physics and Astronomy, University of Alaska Anchorage, 3211 Providence Dr., Anchorage, AK 99508, USA

[4] CTSPS, Clark-Atlanta University, Atlanta, GA 30314, USA

[5] School of Physics and Center for Relativistic Astrophysics, Georgia Institute of Technology, Atlanta, GA 30332, USA

[6] Department of Physics, Southern University, Baton Rouge, LA 70813, USA

[7] Department of Physics, University of California, Berkeley, CA 94720, USA

[8] Lawrence Berkeley National Laboratory, Berkeley, CA 94720, USA

[9] Institut für Physik, Humboldt-Universität zu Berlin, 12489 Berlin, Germany

[10] Fakultät für Physik und Astronomie, Ruhr-Universität Bochum, 44780 Bochum, Germany

[11] Physikalisches Institut, Universität Bonn, Nussallee 12, 53115 Bonn, Germany

[12] Université Libre de Bruxelles, Science Faculty CP230, 1050 Brussels, Belgium

[13] Vrije Universiteit Brussel, Dienst ELEM, 1050 Brussels, Belgium

[14] Department of Physics, Chiba University, Chiba 263-8522, Japan

[15] Department of Physics and Astronomy, University of Canterbury, Private Bag, 4800 Christchurch, New Zealand

[16] Department of Physics, University of Maryland, College Park, MD 20742, USA

[17] Department of Physics, Center for Cosmology and Astro-Particle Physics, Ohio State University, Columbus, OH 43210, USA

[18] Department of Astronomy, Ohio State University, Columbus, OH 43210, USA

[19] Niels Bohr Institute, University of Copenhagen, 2100 Copenhagen, Denmark

[20] Department of Physics, TU Dortmund University, 44221 Dortmund, Germany

[21] Department of Physics, University of Alberta, Edmonton, AB T6G 2E1, Canada

[22] Erlangen Centre for Astroparticle Physics, Friedrich-Alexander-Universität Erlangen-Nürnberg, 91058 Erlangen, Germany

[23] Département de physique nucléaire et corpusculaire, Université de Genève, 1211 Geneva, Switzerland

[24] Department of Physics and Astronomy, University of Gent, 9000 Ghent, Belgium

[25] Department of Physics and Astronomy, University of California, Irvine, CA 92697, USA

[26] Department of Physics and Astronomy, University of Kansas, Lawrence, KS 66045, USA

[27] Department of Astronomy, University of Wisconsin, Madison, WI 53706, USA

[28] Department of Physics, Wisconsin IceCube Particle Astrophysics Center, University of Wisconsin, Madison, WI 53706, USA

[29] Institute of Physics, University of Mainz, Staudinger Weg 7, 55099 Mainz, Germany

[30] Université de Mons, 7000 Mons, Belgium

[31] Technische Universität München, 85748 Garching, Germany

[32] Department of Physics and Astronomy, Bartol Research Institute, University of Delaware, Newark, DE 19716, USA

[33] Department of Physics, University of Oxford, 1 Keble Road, Oxford OX1 3NP, UK

[34] Physics Department, South Dakota School of Mines and Technology, Rapid City, SD 57701, USA

[35] Department of Physics, University of Wisconsin, River Falls, WI 54022, USA

[36] Department of Physics, Oskar Klein Centre, Stockholm University, 10691 Stockholm, Sweden

[37] Department of Physics and Astronomy, Stony Brook University, Stony Brook, NY 11794-3800, USA

[38] Department of Physics, Sungkyunkwan University, Suwon 440-746, Korea

[39] Department of Physics, University of Toronto, Toronto, ON M5S 1A7, Canada

[40] Department of Physics and Astronomy, University of Alabama, Tuscaloosa, AL 35487, USA

[41] Department of Astronomy and Astrophysics, Pennsylvania State University, University Park, PA 16802, USA

[42] Department of Physics, Pennsylvania State University, University Park, PA 16802, USA

[43] Department of Physics and Astronomy, Uppsala University, Box 516, 75120 Uppsala, Sweden

[44] Department of Physics, University of Wuppertal, 42119 Wuppertal, Germany

[45] DESY, 15735 Zeuthen, Germany

Abstract Dark matter which is bound in the Galactic halo might self-annihilate and produce a flux of stable final state particles, e.g. high energy neutrinos. These neutrinos can be detected with IceCube, a cubic-kilometer sized Cherenkov detector. Given IceCube's large field of view, a character-istic anisotropy of the additional neutrino flux is expected. In this paper we describe a multipole method to search for such a large-scale anisotropy in IceCube data. This method uses the expansion coefficients of a multipole expansion of neutrino arrival directions and incorporates signal-specific weights for each expansion coefficient. We apply the technique to a high-purity muon neutrino sample from the Northern Hemisphere. The final result is compatible with the null-hypothesis. As no signal was observed, we present limits on

[a] e-mail: reimann@physik.rwth-aachen.de

[b] Earthquake Research Institute, University of Tokyo, Bunkyo, Tokyo 113-0032, Japan

[c] NASA Goddard Space Flight Center, Greenbelt, MD 20771, USA

the self-annihilation cross-section averaged over the relative velocity distribution $\langle \sigma_A v \rangle$ down to $1.9 \times 10^{-23}\, \mathrm{cm}^3\, \mathrm{s}^{-1}$ for a dark matter particle mass of 700–1,000 GeV and direct annihilation into $\nu\bar{\nu}$. The resulting exclusion limits come close to exclusion limits from γ-ray experiments, that focus on the outer Galactic halo, for high dark matter masses of a few TeV and hard annihilation channels.

1 Introduction

There is compelling evidence for dark matter, e.g. from cosmic microwave background anisotropies, large-scale structure formation, galaxy rotation-curves, and other astrophysical observations [1–3]. Despite this evidence, DM can not be (fully) explained by standard model particles, and its nature remains unknown [3]. Many theories, e.g. supersymmetry or extra dimensions, provide suitable candidates for dark matter [3]. The generic candidate for dark matter is a weakly interacting massive particle (WIMP) with a mass of a few GeV up to several hundred TeV [4,5]. Assuming that WIMPs interact at the scale of the weak force and were produced in the early universe in thermal equilibrium, the freeze-out of WIMPs leads to an expected dark matter abundance that is compatible with current estimates [2].

The density of WIMPs gravitationally trapped as dark halos in galaxies can be high enough that their pair-wise annihilation rate is not negligible. The final-state products of the annihilations decay to stable standard model particles, i.e., photons, protons, electrons or neutrinos, and, therefore, an observable flux of these particles could provide indirect evidence for dark matter. While charged cosmic rays are deflected by magnetic fields and photons have a large astrophysical foreground, astrophysical neutrinos from dark matter annihilation do not interact with inter-stellar matter and would point back to their origin. In certain models, neutrinos can also be produced directly [6], giving a monochromatic neutrino signal that would be a golden channel for neutrino telescopes.

Observations of an excess in the positron to electron ratio by PAMELA [7], that was confirmed by FERMI [8] and AMS-02 [9,10], may hint to dark matter in the GeV–TeV region. The nature of the positron signal is extremely difficult to interpret due to the complex propagation of electrons and positrons in the Galactic magnetic fields. The observation can also be explained by nearby astrophysical sources like pulsars [11] or supernova remnants [12]. However, if the positron excess is interpreted as originating from dark matter, leptophilic dark matter [13,14] is favored, with cross-sections in the range 10^{-24}–$10^{-21}\, \mathrm{cm}^3\, \mathrm{s}^{-1}$, partly within the sensitivity reach of the analysis presented here.

As mentioned above, the annihilation rate is significantly enhanced in regions where DM might have been gravita-

tionally accumulated, since the annihilation rate scales with the square of the density. In particular, massive bodies like the Sun [15], the Earth [16], the Galactic Center [17,18] or dwarf galaxies and galaxy clusters [19], are good candidates to search for a neutrino flux from DM annihilations. Furthermore, and due to the expected shape of the dark halo around the Milky Way, annihilations in the halo would produce a diffuse flux of neutrinos with a characteristic large-scale structure [20], depending on the assumed DM density distribution. While searches for a neutrino flux from the annihilation of DM captured in massive bodies are sensitive to the spin-dependent and spin-independent DM-nucleon cross-section, the Galactic and extra-galactic flux depends on the self-annihilation cross section [3].

In this paper we present a multipole method to search for a characteristic anisotropic flux of neutrinos from dark matter annihilation in the Galactic halo. The method is based on a multipole expansion of the sky map of arrival directions and an optimized test statistic using the expansion coefficients. This method provides the opportunity to reduce the influence of systematic uncertainties in the result, which arise from systematic uncertainties on the zenith dependent acceptance and zenith dependent atmospheric neutrino flux. A large-scale anisotropy as seen by [21–24] in cosmic-rays, is expected in the atmospheric neutrino flux. However this anisotropy is very small so that it is just an effect of few percent compared to our sensitivity on neutrinos from dark matter annihilations.

This paper is organized as follows: In Sect. 2 the IceCube Neutrino Observatory is introduced. Section 3 gives the theoretical expected flux from dark matter annihilation with neutrinos as final state. Section 4 gives a short overview of the data sample used and the simulation of pseudo-experiments. In Sect. 5 the multipole analysis technique is introduced. The sensitivity of this analysis is given in Sect. 6. Section 7 addresses systematic uncertainties. In Sects. 8 and 9 the experimental result is presented and discussed, while in Sect. 10 we present our conclusions.

2 The IceCube Neutrino Observatory

IceCube is a cubic-kilometer Cherenkov neutrino detector located at the geographic South Pole [25]. When a neutrino interacts with the clear Antarctic ice, secondary leptons and hadrons are produced. These relativistic secondary particles produce Cherenkov light which is detected by Digital Optical Modules (DOMs) that contain a photomultiplier tube. The IceCube array consists of 86 strings, each instrumented with 60 DOMs, which are located at depths from 1.45 to 2.45 km below the surface. The strings are arranged in a hexagonal pattern with an inter-string spacing of about 125 m and a DOM-to-DOM distance along each string of 17 m. A more compact sub-array, called DeepCore, consisting of
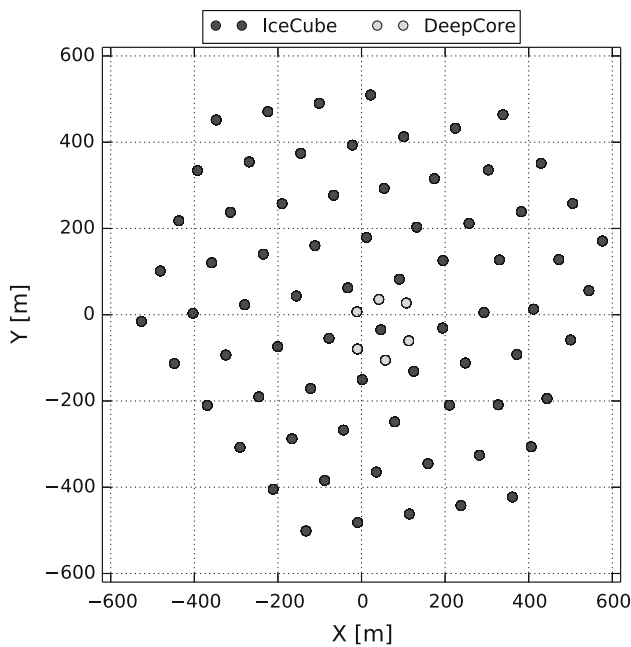
Fig. 1 Footprint of the IceCube detector in its 79-string configuration, that was taking data from June 2010 to May 2011. Shown is the position of the strings, where standard IceCube strings are marked in *dark gray*, and DeepCore strings with a smaller DOM spacing are marked in *light gray*

eight densely-instrumented strings, has been embedded in the center of IceCube in order to lower the energy threshold from about 100 to about 10 GeV [26]. The detector construction was completed in December 2010, however data were already taken with partial configurations [27]. The footprint of IceCube in its 79-string configuration (IC79) is shown in Fig. 1. This is the configuration used in this analysis. Due to its unique position at the geographic South Pole, the zenith angle in local coordinates is directly related to the declination and the right ascension for a given azimuth angle only depends on the time.

3 Neutrino flux from dark matter annihilation in the Galactic halo

N-body simulations [28–30] predict the mass distribution $\rho_{DM}(r)$ in galaxies as function of the distance r to the Galactic Center, assuming a spherically symmetric distribution. The resulting dark matter halo profile is parameterized by an extension of the Hernquist model [31]

$$\rho_{DM}(r) = \frac{\rho_0}{\left(\delta + \frac{r}{r_s}\right)^\gamma \cdot \left[1 + \left(\frac{r}{r_s}\right)^\alpha\right]^{(\beta-\gamma)/\alpha}}, \quad (1)$$

where $(\alpha, \beta, \gamma, \delta)$ are dimensionless parameters. r_s is a scaling radius and ρ_0 is the normalization density. Both have to be determined for each galaxy.
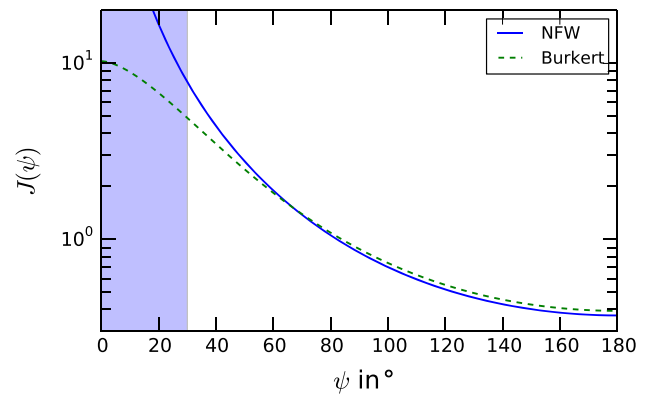

Fig. 2 Line of sight integral $J(\psi)$ as function of the angular distance ψ to the Galactic Center is shown for the different halo profiles used in this analysis. The *shaded region* corresponds to angular distances to the Galactic Center that lie in the Southern Hemisphere and are not used in this analysis

In this paper the halo profile of Navarro, Frenk and White (NFW) [32,33] with $(1, 3, 1, 0)$ is used as baseline. For the Milky Way $r_s = 16.1^{+17.0}_{-7.8}$ kpc and $\rho(r_s) = 0.47^{+0.05}_{-0.06}$ GeV/cm^3 are used [34]. A currently favored model is the Burkert profile, that was obtained by the observation of dark matter dominated dwarf galaxies. The Burkert profile is described by $(2, 3, 1, 1)$ [35], $r_s = 9.26^{+5.6}_{-4.2}$ kpc and $\rho(r_s) = 0.49^{+0.07}_{-0.09}$ GeV/cm^3 [34]. While for the central part of the galaxy the models differ by orders of magnitude, the outer profiles are rather similar.

The expected differential neutrino flux $d\phi_\nu/dE$ at Earth depends on the annihilation rate $\Gamma_A = \langle\sigma_A v\rangle\rho(r)^2/2$ along the line of sight l, the muon neutrino yield per annihilation dN_ν/dE, and the self-annihilation cross-section of dark matter averaged over the velocity distribution $\langle\sigma_A v\rangle$. The flux is given by [36]:

$$\frac{d\phi_\nu}{dE} = \frac{\langle\sigma_A v\rangle}{2} J(\psi) \frac{R_{SC}\rho_{SC}^2}{4\pi m_\chi^2} \frac{dN_\nu}{dE}, \quad (2)$$

where m_χ denotes the mass of the dark matter particle. $J(\psi)$ is the dimensionless line of sight integral, that depends on the angular distance to the Galactic Center, ψ, and is defined by [36]:

$$J(\psi) = \int_0^{d_{max}} dl \frac{\rho_{DM}^2\left(\sqrt{R_{SC}^2 - 2lR_{SC}\cos\psi + l^2}\right)}{R_{SC}\rho_{SC}^2}, \quad (3)$$

where ρ_{DM}^2 is evaluated along the line of sight, that is parameterized by $\sqrt{R_{SC}^2 - 2lR_{SC}\cos\psi + l^2}$ and ρ_{SC} is the local dark matter density at the distance $R_{SC} = 8.5$ kpc of the Sun from the Galactic Center [36]. d_{max} is the upper boundary of the integral and is sufficiently larger than the size of the galaxy. The dimensionless line of sight integral for different halo profiles is shown in Fig. 2. A large difference for small

angles ψ can be seen, while for the outer part a similar factor is expected for all models.

This analysis searches for an anisotropy in the neutrino arrival directions on the Northern Hemisphere. Here we expect a characteristic anisotropy, proportional to $J(\psi)$ as shown in Fig. 3.

The neutrino multiplicity per annihilation for the flavors e, μ, τ, are obtained with DarkSUSY, which is based on Pythia6 [20,37]. The muon neutrino multiplicity per annihilation at Earth, dN_ν/dE, includes the oscillation probability into muon neutrinos in the long baseline limit. The effective oscillation probability was calculated by numerical averaging of the oscillation probability over a sufficient number of oscillation length using mixing angles and amplitudes from [38]. Since the nature of the DM particles, as well as the branching ratio for different annihilation channels, are
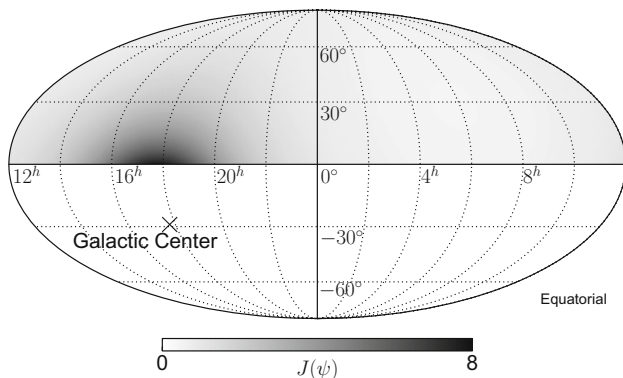

Fig. 3 Dimensionless line-of-sight integral for the NFW profile is shown for the Northern Hemisphere in equatorial coordinates. The anisotropy in the line-of-sight integral causes the anisotropy in the expected flux of neutrinos from self-annihilation of dark matter in the Galactic halo. The position of the Galactic Center is indicated by the *cross*
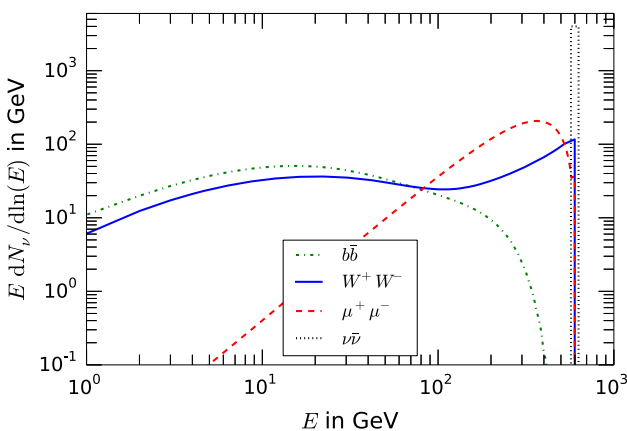

Fig. 4 Muon neutrino multiplicity per annihilation $dN_\nu/d\ln(E)$ as function of energy is shown for the investigated benchmark channels and $m_\chi = 600$ GeV. The oscillation probability into muon neutrinos, in the long baseline limit, is included in $dN_\nu/d\ln(E)$. Beside the neutrino line spectrum, the spectra were calculated with DarkSUSY [37]

unknown, a 100 % branching ratio to a few benchmark channels is assumed. Similar to previous analyses [19], we use the annihilation to $b\bar{b}$ as a soft channel, W^+W^- as a medium and $\mu^+\mu^-$ as a hard channel. Furthermore we investigate direct annihilation to $\nu\bar{\nu}$, which results in a line spectrum. We assume a 1:1:1 neutrino flavor at source, and then use the long-baseline approximation as for all other spectra. This model is implemented as a uniform distribution within ± 5 % of m_χ, instead of a Dirac delta-distribution, for computational reasons. The different muon neutrino multiplicity per annihilation spectra $E^2 dN_\nu/dE = E \cdot dN_\nu/d\ln(E)$ are shown in Fig. 4.

4 Data sample

4.1 Experimental data

Data taken from June 2010 to May 2011, with a total live-time T_{live} of 316 days, are used. Up-going muon events (declination >0) were selected in order to eliminate atmospheric muon background, which becomes dominant at a few degrees above the horizon. By means of a mixture of one dimensional cuts on event quality parameters and a selection by a boosted decision tree [39] the contamination of misreconstructed atmospheric muons that mimic up-going neutrinos was reduced to <3 % [40]. The detailed selection is described in [41] as "Sample B" for IC79. After the rejection of atmospheric muons, the sample consists of 57281 up-going muon events from the Northern Hemisphere, mostly atmospheric muon neutrinos, which are background for the search of neutrinos from self-annihilating dark matter in the Galactic halo. Unlike signal, the integrated atmospheric neutrino flux is nearly constant with right ascension [20]. The reconstructed arrival directions of all events in the final sample are shown in Fig. 5. From full detector simulation it was found that 90 % of the events have a neutrino energy in the range from about 100 GeV to about 10 TeV, with a median of 613 GeV.
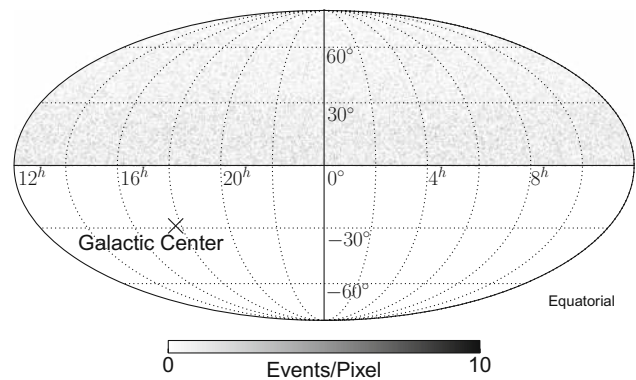

Fig. 5 Sky map of reconstructed neutrino arrival direction of the experimental data sample in equatorial coordinates. The position of the Galactic Center is indicated by the *cross*

The median angular resolution is $<1°$ for energies above 100 GeV [41]. Further details on the sample properties can be found in [41].

4.2 Pseudo-experiments

The sensitivity of this analysis has been estimated and optimized by pseudo experiments with simulated sky maps of neutrino arrival directions. These sky maps contain background from atmospheric neutrinos and misreconstructed atmospheric muons and signal from dark matter annihilation.

Signal events are generated at a rate proportional to the line-of-sight integral. Furthermore, the arrival direction is smeared according to the angular resolution [20], which was determined with the full detector simulation. Moreover, the acceptance of each event is randomized according to the declination-dependent effective area. It is assumed that the acceptance is constant in RA, due to IceCube's special position at the South Pole and the daily rotation of the Earth and the almost continuous operation of the detector, which results in a livetime of 91 % at final selection level.

The background generation is done by scrambling experimental data. Here, the declination of the experimental events are kept and the RA is uniformly randomized. The rescrambling of experimental data to generate background is justified by a negligible signal contamination in the experimental data. By this technique the background estimation is not affected by systematic uncertainties from Monte-Carlo simulation.

The number of signal events in a sky map is fixed to N_{sig}. The total number of events in a sky map N_ν is fixed to the total number of events in the experimental sample, so that the sky maps are filled up with $N_\nu - N_{sig}$ background events.

5 Method

5.1 Multipole expansion of sky maps

The sky maps of reconstructed neutrino arrival directions are expanded by spherical harmonics Y_ℓ^m [42]. Spherical harmonics are given by

$$Y_\ell^m(\theta, \phi) = \sqrt{\frac{(2\ell + 1)(\ell - m)!}{4\pi(\ell + m)!}} P_\ell^m\left(\cos\left(\frac{\pi}{2} - \theta\right)\right) e^{im\phi},$$
(4)

where θ is the declination and ϕ the RA. ℓ, m are integer numbers with $0 \leq \ell$ and $-\ell \leq m \leq \ell$. P_ℓ^m are the associated Legendre polynomials. Because spherical harmonics are a complete set of orthonormal functions, one can expand all square-integrable functions $f(\theta, \phi)$ on a full sphere Ω into spherical harmonics. The expansion is given by

$$f(\theta, \phi) = \sum_\ell \sum_{m=-\ell}^{m=\ell} a_\ell^m \cdot Y_\ell^m(\theta, \phi)$$
(5)

with expansion coefficients a_ℓ^m. Here, ℓ is the order of the expansion and corresponds to an angular scale of approximately $180°/\ell$, while m corresponds to the orientation of the spherical harmonic. The expansion coefficients are given by

$$a_\ell^m = \int_\Omega d\Omega \, f(\theta, \phi) \, Y_\ell^{m*}(\theta, \phi).$$
(6)

The sky map of reconstructed arrival directions is represented by

$$f(\theta, \phi) = \sum_{i=1}^{N_\nu} \delta^D(\cos(\theta) - \cos(\theta_i)) \cdot \delta^D(\phi - \phi_i),$$
(7)

where (θ_i, ϕ_i) are reconstructed coordinates of event i in equatorial coordinates. N_ν is the total number of events in the data sample and δ^D is the Dirac-delta-distribution. Since the median angular resolution of the events $(<1°)$ is much smaller than the anisotropy to search for, the usage of Dirac-delta-distributions is justified.

Coefficients with negative m do not provide additional information, because the sky map is described by a real function, leading to $|a_\ell^m| = |a_\ell^{-m}|$, and a fixed relation between $\arg(a_\ell^m)$ and $\arg(a_\ell^{-m})$ [42].

The multipole expansion is linear and the expansion coefficients for signal and background follow the superposition principle. This can be seen from Eq. (6), if one uses $f(\theta, \phi) = s \cdot f_{sig}(\theta, \phi) + (1-s) \cdot f_{bgd}(\theta, \phi)$, where $f_{sig}(\theta, \phi)$ is the sky map for pure signal, $f_{bgd}(\theta, \phi)$ is the sky map for pure background, and s is the relative signal strength.

In practice the expansion is stopped at some large ℓ_{max}. Information on structures of an angular scale smaller $180°/\ell$ will be lost. Hence, the value of ℓ_{max} should be sufficiently large to include all angular scales of interest.

5.2 Application of multipole-expansion to pseudo-experiments

For this analysis the calculation of the expansion coefficients is done with the software package HealPix [43,44].

Figures 6 and 7 show the expansion coefficient corresponding to Y_ℓ^m with $\ell = 2$ and $m = 1$ for a signal, as described in Sect. 3, and a uniform distributed background in RA, as described in Sect. 4.

For different signal strength $s = N_{sig}/N_\nu$, 1,000 pseudo-experiments were performed and a_2^1 was calculated. For pure background sky maps ($s = 0$ %) with no preferred direction in RA (uniform) the expansion coefficient shows no preferred phase and is almost normal distributed around the origin of
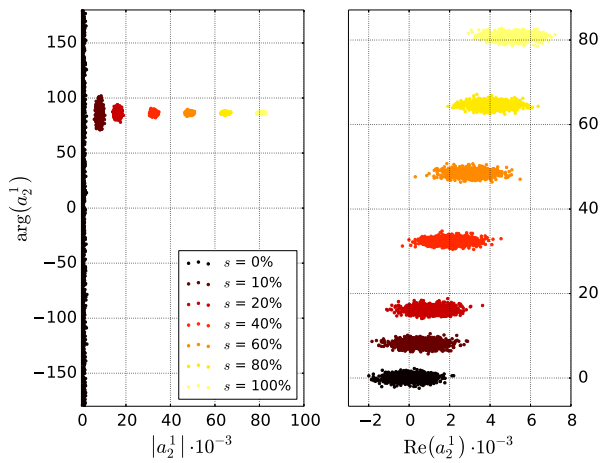
Fig. 6 The expansion coefficient a_2^1 for large signal strength s in the Euler representation (*left panel*) and in the complex plane (*right panel*). For each signal strength s 1,000 pseudo-experiments were generated and the expansion coefficient a_2^1 calculated
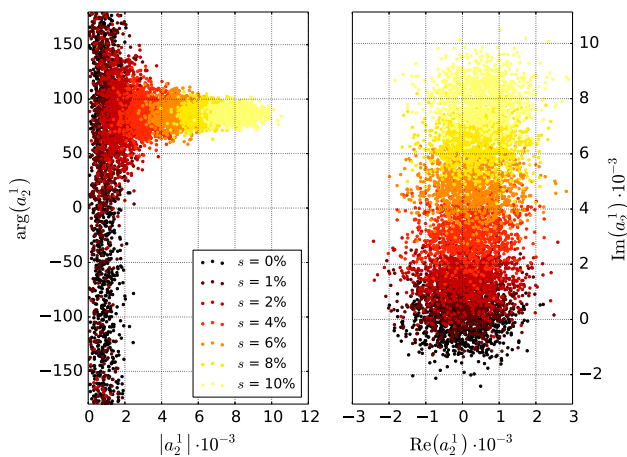

Fig. 7 The expansion coefficient a_2^1 for small signal strength s in the Euler representation (*left panel*) and in the complex plane (*right panel*). For each signal strength s 1,000 pseudo-experiments were generated and the expansion coefficient a_2^1 calculated
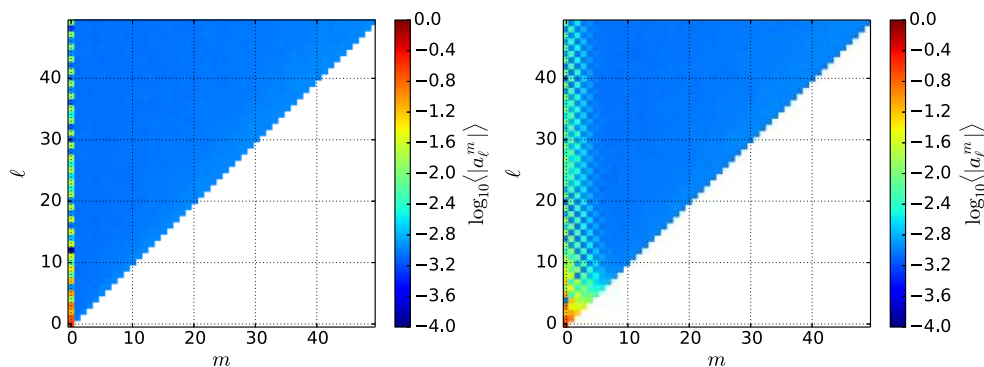
the complex plane. For pure signal ($s = 100\%$) there is a clear separation from the origin. Also, a clear preferred phase can also be observed, which corresponds to the orientation of the expected anisotropy in the sky. This phase is the same as the preferred phase for the sky maps with partial signal ($0\% < s < 100\%$). Furthermore, a linear dependency between the signal strength s and the mean power $\langle|a_2^1|\rangle$ can be seen.

In practice the number of events N_ν in the map is limited. Therefore, the value of a_ℓ^m has a statistical error, which depends on the total number of events in the sky map N_ν and weakly on the signal fraction s. For the value $N_\nu > 57,000$ of this analysis the error can be well approximated as Gaussian.

An overview of the logarithm of the absolute value of all expansion coefficients with $0 \leq \ell, m \leq 50$ is shown in Fig. 8 for pure background (left panel), and pure signal (right panel). For the pure background case most of the power is contained in the coefficients a_ℓ^0, related to the pure zenith structure. Because the background was assumed to be isotropic in RA all coefficients with $m \neq 0$ are at noise level. The statistical noise level in the map is of the order of 10^{-3}–10^{-4} and corresponds to the width of the distribution, as shown in Figs. 6 and 7.

From Eq. (4) one can see that spherical harmonics with $m = 0$ are independent of RA and thus purely depend on declination. The a_ℓ^0 coefficients have an absolute value larger than the noise level that means they contain power. These coefficients describe the full declination structure, that is mainly influenced by the declination-dependent acceptance and the declination-dependent variation of the atmospheric neutrino flux. Furthermore it was found that there is no preferred phase in any coefficient for background.

For pure signal (Fig. 8, right) there is also power in coefficients with $m \neq 0$, resulting from the characteristic anisotropy of the signal. It was found that all coefficients that have a power larger than the noise level also have a preferred phase. The characteristic checkered pattern in the coefficients
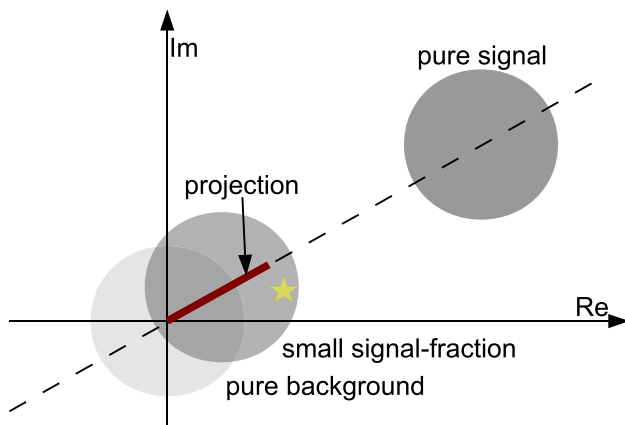

Fig. 8 Mean logarithm of the absolute value for all expansion coefficients in the ℓ–m-plane up to $\ell, m = 50$. The mean absolute value was obtained from 1,000 pure background/signal sky maps (*left/right*)

Fig. 9 Sketch to illustrate the projection of complex expansion coefficients, on the axis corresponding to the preferred direction. The *large gray circles* represent the central part of the Gaussian in the complex plane in a large ensemble limit for different signal strength. In contrast to that distributions the *star* corresponds to one specific value of the expansion coefficient for one measured sky map. The projected value of this specific expansion coefficient is given by the *length of the thick red line*

results from the observation of just one hemisphere $\theta > 0$, leading to a suppression of coefficients with even $\ell + m$, that correspond to a symmetric spherical harmonic with respect to the equator.

From Fig. 8 (right panel) it becomes obvious that coefficients with small ℓ and m carry most power. This is due to the large-scale anisotropy of the line-of-sight integral (see Fig. 3). In analogy to the relation of ℓ and the characteristic angular scale of the structure, m is related to the characteristic angular scale in RA, thus small m represent large structures in RA and large m represent small structures in RA.

5.3 Test statistic

The test statistic (TS) to separate signal from background combines the phase information and the power of a complex coefficient into one value. A projection of the complex coefficient onto the axis, corresponding to the preferred phase, is introduced [45]. This projection is illustrated in Fig. 9 and is given by

$$\mathcal{A}_\ell^m = \|a_\ell^m\| \cos\left(\arg\left(a_\ell^m\right) - \left\langle\arg\left(a_{\ell,\mathrm{sig}}^m\right)\right\rangle\right),\qquad(8)$$

where $\arg\left(a_\ell^m\right)$ is the argument of a_ℓ^m and $\langle\arg(a_{\ell,\mathrm{sig}}^m)\rangle$ is the mean expected phase of the a_ℓ^m of pure signal pseudo-experiments.

This projected expansion coefficient has the following advantages. First $\mathcal{A}_\ell^m$ is proportional to the power of the expansion coefficient. Second, the most sensitive direction is the axis of the preferred phase, and the value of the projection gets smaller, the more the phase differs. This results in

negative values for $\mathcal{A}_\ell^m$, if the phase differs more than $\pi/2$, indicating that the anisotropy is in the opposite direction of the expectation.

Using these projected expansion coefficients the TS is defined as

$$TS = \frac{1}{\sum w_\ell^m} \sum_{\ell=1}^{\ell_{\max}} \sum_{m=1}^{\ell} \mathrm{sig}\left(\mathcal{A}_\ell^m\right) w_\ell^m \left(\frac{\mathcal{A}_\ell^m - \left\langle\mathcal{A}_{\ell,\mathrm{bgd}}^m\right\rangle}{\sigma\left(\mathcal{A}_{\ell,\mathrm{bgd}}^m\right)}\right)^2$$
$$(9)$$

where $\mathrm{sig}(x)$ gives the sign of x and $\langle\mathcal{A}_{\ell,\mathrm{bgd}}^m\rangle$ and $\sigma(\mathcal{A}_{\ell,\mathrm{bgd}}^m)$ are the mean and standard deviation of an ensemble of $\mathcal{A}_\ell^m$ estimated from pseudo-experiments of pure background [45]. w_ℓ^m are individual weights for each coefficient. The definition of the test statistic is motivated by a weighted χ^2-function. The weights are chosen with respect to the separation power of the different coefficients and are defined below. Because the sign of the deviation is lost in the squared term, the sign is included as an extra factor. Coefficients with no power, especially in the background case, have randomly positive or negative sign. In average they add up to zero, however for signal always positive values contribute to the sum.

The weights are given by

$$w_\ell^m = \left|\frac{\left\langle\mathcal{A}_{\ell,\mathrm{sig}}^m\right\rangle - \left\langle\mathcal{A}_{\ell,\mathrm{bgd}}^m\right\rangle}{\sigma\left(\mathcal{A}_{\ell,\mathrm{bgd}}^m\right)}\right|,\qquad(10)$$

where $\langle\mathcal{A}_{\ell,\mathrm{sig}}^m\rangle$ is the expected projected expansion coefficient for pure signal, that can be calculated by averaging over the $\mathcal{A}_\ell^m$ of an ensemble of pseudo-experiments for pure signal. Because $\mathcal{A}_\ell^m$ is proportional to a_ℓ^m and, thus, to the signal strength, a smaller signal expectation would just lead to a different normalization of the weight, which is absorbed in the factor $1/\sum w_\ell^m$. Therefore the relative strength of coefficients in this test statistic does not depend on the signal strength s. The weights represent the power to separate signal from background for each coefficient. Insensitive expansion coefficients get assigned a small weight and do not contribute.

5.4 Test statistic application to the search for dark matter

To determine $\langle\arg(a_{\ell,\mathrm{sig}}^m)\rangle$, w_ℓ^m, $\langle\mathcal{A}_{\ell,\mathrm{bgd}}^m\rangle$ and $\sigma(\mathcal{A}_{\ell,\mathrm{bgd}}^m)$, 1,000 pseudo-experiments were used in each case. The weights for an NFW profile for all coefficients with $\ell, m \leq 100$ are shown in Fig. 10.

The weights range over orders of magnitude and are proportional to the values shown in Fig. 8 (right panel) reflecting the separation power of the coefficients.
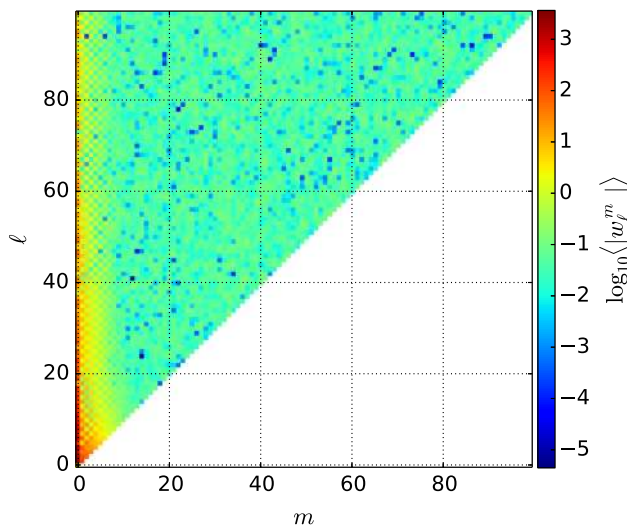
Fig. 10 The logarithm of the weight [as defined in Eq. (10)] for all coefficients in the ℓ–m-plane up to $\ell, m = 100$. In the calculation the NFW profile was used

Fig. 11 Test statistic TS for pure background simulation (*solid*) and simulations with small signal contributions assuming a NFW profile. N_{sig} is the number of simulated neutrino arrival directions from dark matter annihilation in the Galactic halo

For IceCube, the coefficients with $m = 0$ contain the declination dependence and, due to the detector location at the geographic South Pole, this translates directly into the zenith dependence of the detector acceptance. In order to avoid introducing a zenith-dependent systematic uncertainty, the coefficients with $m = 0$ are omitted in this analysis and are not included in Eq. (9). Since spherical harmonics are orthonormal functions, no additional systematic is introduced by this choice. Possible systematic uncertainties in azimuth average out due to the daily rotation of Earth, and thus the detector.

Because the anisotropy introduced by the flux from dark matter annihilation in the halo is a large scale anisotropy a maximal expansion order of $\ell_{\text{max}} = 100$ was chosen. In general the coefficients become less sensitive with lager ℓ. Due to this generic suppression of insensitive coefficients in the test statistic ℓ_{max} does not need to be optimized.

Since the differences in weights for different halo profiles are found to be small, which is a result of the similar shapes of the outer halo predicted by the different models (see Fig. 2), weights from NFW profiles are used for all model tests to avoid trial factors. Differences with respect to the halo profiles will be discussed below.

Figure 11 shows the resulting test statistic for pseudo-experiments of pure background ($N_{\text{sig}} = 0$, $s = 0\%$) and pseudo-experiments with signal contribution of $N_{\text{sig}} = 1,000, 5,000$ (signal strength $s = 1.7, 8.7\%$) assuming a NFW profile.

5.5 Generalization of the method

In the previous sections the assumed signal was the characteristic anisotropy of the flux from dark matter annihilation.
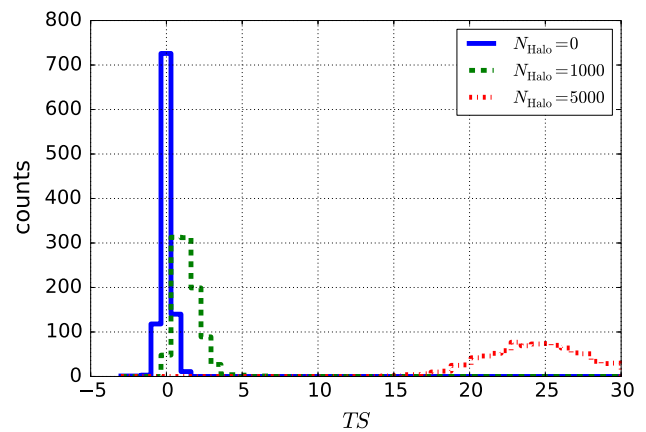
However, the method described here can be generalized to any other anisotropy of preferred direction.

If there is no preferred direction in the signal expectation, i.e. a characteristic event correlation structure which is distributed isotropically on the sky, the phase is also random in the signal case. This is the case e.g. in a search for many point-like sources that are too weak to be detected individually, but which lead to a clustering of events on specific angular scales. Even in these cases it is possible to define a test statistic analogously. Here one can use the averaged power on a characteristic scale C_ℓ^{eff}, that is given by

$$C_\ell^{\text{eff}} = \frac{1}{2\ell} \sum_{\substack{m=-\ell \\ m \neq 0}}^{\ell} \left| a_\ell^m \right|^2. \tag{11}$$

Note that also here the power coefficients are defined without the a_ℓ^0 coefficients, resulting in coefficients that are not affected by systematic uncertainties in the declination acceptance. In the test statistic [Eq. (9)] one has to replace all $\mathcal{A}_\ell^m$ by C_ℓ^{eff} and w_ℓ^m by w_ℓ and remove the sum over m. Furthermore the sig($\mathcal{A}_\ell^m$)-term now has to be written as sig($C_\ell^{\text{eff}} - C_{\ell,\text{bgd}}^{\text{eff}}$). The weight w_ℓ can be defined similar to Eq. (10) by replacing $\mathcal{A}_\ell^m$ by C_ℓ^{eff}. An example where such a test statistic has been used is [46,47].

6 Sensitivity

The median sensitivity at a 90 % confidence level (CL), N_{90}, is given by that number of signal events, where 50 % of the signal TS distribution is larger than the 90 % upper quantile of the background distribution. To estimate this median sensitivity for different signal contributions 25,000 pseudo-
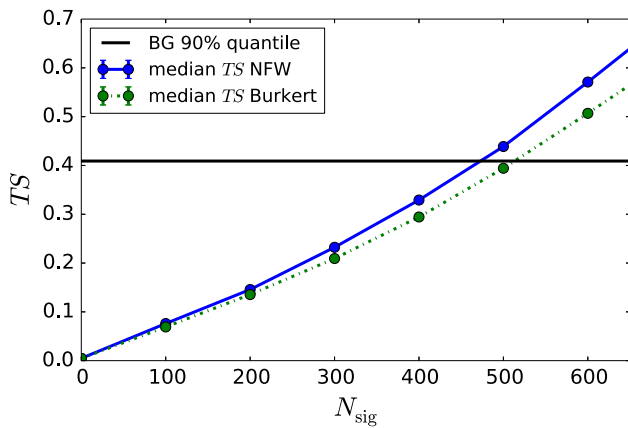
Fig. 12 The median of the test statistic, TS, distribution as a function of the signal strength N_{90} for different halo profiles. Furthermore the 90 %-upper-quantile of the TS background distribution is shown. The statistical errors were computed by binomial statistics and are smaller than the size of the markers

Fig. 13 Effective area as a function of neutrino energy, averaged over declination in the Northern Hemisphere. The *gray band* represents the uncertainties due to systematic uncertainties in the optical detection efficiency and in the ice properties

Table 1 Median sensitivity on the number of signal events at a 90 % CL N_{90} and the statistical uncertainty for different halo profiles

Halo profile	N_{90}
NFW	470.8 ± 2.3
Burkert	511.2 ± 2.8

experiments were generated for different numbers of signal events N_{sig}. In Fig. 12 the median of each TS distribution is shown versus the signal strength N_{sig} for the different halo profiles. Further, the 90 %-quantile of the background distribution is shown. The resulting N_{90} for the different halo profiles are shown in Table 1. It can be seen that differences in the value of N_{90} are smaller than 10 %. Note that the N_{90} value does not depend on the overall normalization but only on the different shape of the profiles.

The sensitivity on the number of signal events in the data set, and thus the flux, can be interpreted in terms of the self-annihilation cross-section of the dark matter. Using Eq. (2) the self-annihilation cross-section is given by

$$\langle \sigma_A v \rangle = \frac{8\pi m_\chi^2}{R_{SC} \rho_{SC}^2} \frac{1}{T_{live}} \frac{1}{\int \int J(\psi) A_{eff} \frac{dN_\nu}{dE} dE d\Omega} N_{90} . \quad (12)$$

Here, A_{eff} is the effective area, which is shown for the chosen data set, averaged over the Northern Hemisphere, in Fig. 13. The resulting sensitivity on the self-annihilation cross-section depends on the assumed annihilation channel and WIMP mass.

In N-body simulations of structure formation using DM, self-similar substructures are found. These structures lead to an enhanced annihilation probability, because the gain of flux from denser regions is larger than the loss in dilute regions. The increas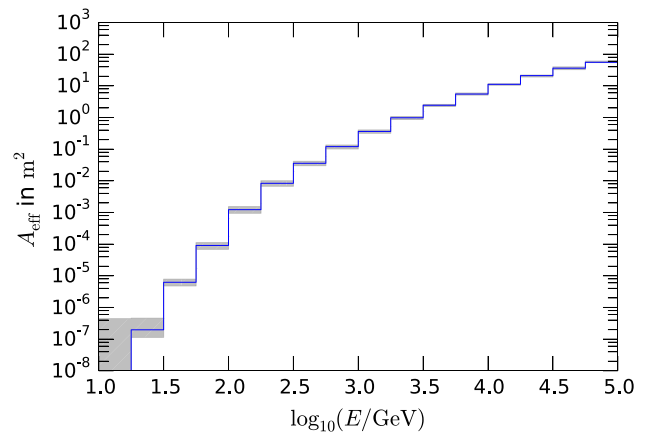e of the annihilation rate can be described by a boost factor $B(r)$, which modifies the line of sight integral. An example of such a boost factor is given in [48] and has been discussed in [20]. For this analysis the modification of the line-of-sight integral as described in [20] results in a median sensitivity, N_{90}, which is about 50 % worse, because the shape of the line-of-sight integral and thus the anisotropy becomes flatter. However, due to the larger total expected flux the sensitivity on the self-annihilation cross-section is 20 % more stringent. To be conservative, the results presented here do not take substructures into account.

As a cross-check, the sensitivity on the number of signal events of a cut-and-count based method as described in [20] was determined. About 14,600 neutrinos are expected in the off-source region, which covers 1.6 sr. This results in a sensitivity to approximately 219 neutrinos when subtracting the number of events in the on-source and off-source regions. Taking into account the different solid angles in the denominator of Eq. (12), 12 % more signal events over background are required for the same significance, resulting in a slightly less sensitive analysis.

7 Systematic uncertainties

The relevant systematic uncertainties for the analysis can be categorized into three groups:

- Systematic uncertainties on the background expectation.
- Systematic uncertainties on the signal detection efficiency.
- Dependencies on the halo profile.

As the background expectation is generated from scrambled experimental events in RA, systematic effects can only

Table 2 Systematic uncertainties resulting from pre-existing anisotropies in the experimental sky map. $\langle\sigma_A v\rangle_{\text{base}}$ denotes $\langle\sigma_A v\rangle$ assuming no pre-existing anisotropy and $\langle\sigma_A v\rangle_{\text{syst}}$ assuming the N_{90} changed by the systematic effects

Uncertainty	$\frac{\langle\sigma_A v\rangle_{\text{syst}}-\langle\sigma_A v\rangle_{\text{base}}}{\langle\sigma_A v\rangle_{\text{base}}}$ (%)
Zenith acceptance	<4.3
Sky exposure	±2.2
Cosmic ray anisotropy	±5.4

be caused by pre-existing anisotropies. Such an anisotropy can arise from the zenith-dependent acceptance of the detector, the zenith-dependent variation of the atmospheric neutrino flux or the detector exposure. There is also the possibility of an anisotropy in the atmospheric neutrino flux, caused by the cosmic-ray anisotropy which has been measured by Milagro [21], TUNKA [22], ARGO-YBJ [24] and IceCube [23].

The systematic uncertainty on the self-annihilation cross-section caused by zenith-dependent uncertainties is very small as a result of the fact that the coefficients corresponding to pure zenith(declination)-dependent spherical harmonics are not included in the test statistic. In order to study the influence of the zenith structure that arises from the acceptance of the detector and the variation of the atmospheric neutrino flux, pseudo-experiments were generated using events according to a histogram of experimental zenith values and not using the experimental data directly. To generate steeper and flatter zenith-spectra, the bin-contents of the histogram are changed by raising the outer most left bin by 25 % and decreasing the outer most right bin by 25 %. The bins in between are raised or decreased according to a linear interpolation between +25 % and −25 %. The uncertainties on the zenith-spectrum are on the order of 5 %. However to study this effect and not be limited by statistics the slope of the zenith-spectrum was changed by ±50 % resulting in a large overestimation of the effect. Based on these pseudo-experiments the median sensitivity on $\langle\sigma_A v\rangle$ was calculated. This results in a conservative upper limit on the effect of zenith-dependent uncertainties (see Table 2).

The up-time of the IceCube-detector is of the order of 98 %, however due to high quality criteria in the data selection the used data correspond to 91 % up-time. The geometry of the detector is almost symmetric in azimuth, and thus the exposure of each direction in the sky is nearly constant. However due to short down-times and a non flat azimuth acceptance an anisotropy of 0.02 % in the data sample (∼10 events) can occur. In the worst case this anisotropy can mimic a (anti-)signal and thus result in a small systematic effect on the median sensitivity $\langle\sigma_A v\rangle$ (see Table 2).

Milagro, ARGO-YBJ and TUNKA have observed an anisotropy in cosmic rays at few hundred GeV–EeV energies of primary particles in the Northern Hemisphere [21,22,24]. Because the experimental sky map is dominated by atmospheric neutrinos, that were produced in air-showers initiated by cosmic rays an analogous anisotropy is expected in atmospheric neutrinos. Therefore, pseudo-experiments were generated that allow for an anisotropy as parameterized in [21]. The uncertainty on the median sensitivity on $\langle\sigma_A v\rangle$ is given in Table 2.

Systematic uncertainties on the signal efficiency can be expressed by uncertainties in the effective area. Because the effective area depends on energy, the resulting systematic uncertainties on $\langle\sigma_A v\rangle$ depend on the assumed energy-spectrum and, thus, on the annihilation channel and the mass of the dark matter particle.

The main uncertainties of the detection efficiency arise from the optical efficiency of the DOMs and from the optical properties of the antarctic ice, described by the absorption and scattering length. The influence of these effects on the effective area was determined by a full detector simulation where

Table 3 Relative systematic uncertainties on $\langle\sigma_A v\rangle$ resulting from uncertainties in the detection efficiency. Because the detection efficiency is energy-dependent, the uncertainties are given in dependence of annihilation channel and the mass of the DM particle m_χ. $\langle\sigma_A v\rangle_{\text{base}}$ denotes $\langle\sigma_A v\rangle$ assuming the baseline effective area and $\langle\sigma_A v\rangle_{\text{syst}}$ assuming the effective area changed by the systematic effects

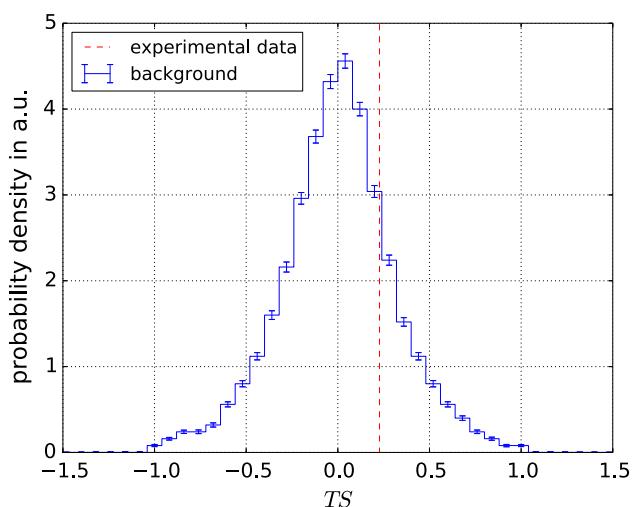| m_χ (GeV)	$\frac{\langle\sigma_A v\rangle_{\text{syst}}-\langle\sigma_A v\rangle_{\text{base}}}{\langle\sigma_A v\rangle_{\text{base}}}$ (%)			
	$b\bar{b}$	W^+W^-	$\mu^+\mu^-$	$\nu\bar{\nu}$
100	±89	±30	±32	±33
200	±34	±28	±30	±29
300	±26	±25	±27	±24
400	±27	±22	±24	±15
500	±27	±20	±22	±18
600	±26	±19	±20	±22
700	±25	±18	±19	±15
800	±25	±18	±19	±17
900	±24	±18	±18	±18
1,000	±23	±18	±18	±14
2,000	±20	±15	±16	±12
3,000	±19	±14	±14	±16
4,000	±18	±13	±13	±15
5,000	±18	±12	±12	±13
10,000	±16	±10	±11	±9
20,000	±14	±9	±7	±12
30,000	±13	±10	±8	±10
50,000	±12	±7	±7	±24
70,000	±11	±6	±4	±13
10,0000	±10	±6	±3	±26

Fig. 14 TS distribution for background expectation (*solid*), and the observed value $TS_{exp} = 0.23$ (*dashed*). The *error bars* on the background distribution reflect the statistical precision arising from the finite number of pseudo-experiments realized
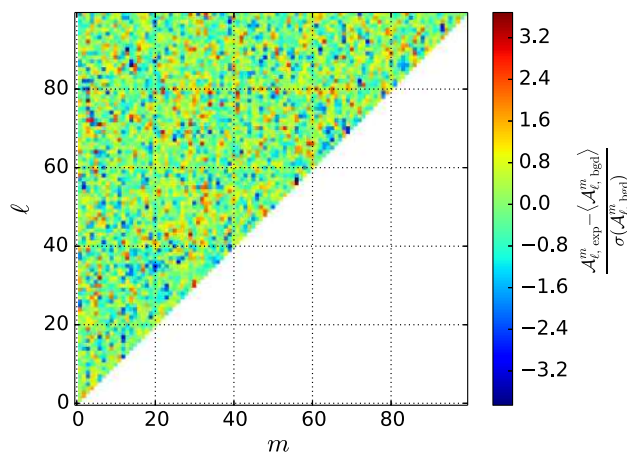

Fig. 15 Deviation of experimental projected expansion coefficients from background expectation, normalized to standard deviation of background coefficients in the ℓ–m-plane. No significant excess can be seen

the nominal values of the DOM efficiency and the absorption and scattering lengths were changed by $\pm 10\%$ [49,50]. The uncertainties on the effective area were further propagated to uncertainties on $\langle \sigma_A v \rangle$, which depends on the dark matter particle mass m_χ and the annihilation channel. The resulting uncertainties are listed in Table 3. They typically lie in the range 15–30 %, and they are the dominating uncertainties of this analysis.

The sensitivities as obtained from the different halo profiles using best-fit parameters differ by about 6 %. This is smaller than the uncertainty that arises from uncertainties on the profile fit values. The dominant contribution comes from the local dark matter density, and corresponds to an uncertainty on the sensitivity of up to 50 %. In the following the dependency of the assumed model is not treated as a systematic uncertainty, but as model uncertainty, and thus the experimental result will be interpreted for each of the different halo profiles, and benchmark annihilation channels, respectively.

8 Experimental results

This analysis was performed blind, meaning it was developed by using pseudo-experiments only. After the analysis procedure was optimized and fixed, the data were unblinded. The experimental sky map has a test statistic value of $TS_{exp} = 0.23$. The probability of a larger experimental value in the background-only case is 22 % and thus the result is compatible with the background-only hypothesis. The observation is an over-fluctuation corresponding to 0.8σ, where σ is the standard deviation of the background expectation of the test

statistic. Note that the test statistic can not be approximated by a Gaussian due to larger tails. The experimental value and the background expectation of the test statistic are shown in Fig. 14.

Figure 15 shows the deviation of the experimental expansion coefficients from the background expectation, normalized to the standard deviation of the background coefficients. These values correspond to the last term in Eq. (9) without the square. Also here no significant deviation can be seen.

As no signal was observed, upper limits on the number of signal events in the sample, N_{UL}, were calculated at a 90 % CL following the approach of Feldman and Cousins [51]. In order to calculate the confidence belt, 25,000 pseudo-experiments for different N_{sig} were generated respectively. Due to limited computational resources the pseudo-experiments were not generated for each N_{sig}, but for signal contributions $N_{sim,i}$ with a step-size of $\Delta_{sim} = 25$ events. The test statistic distribution was interpolated for the remaining N_{sig}, using a Gaussian, p_{gaus}, with mean $\mu = N_{sig}$ and standard deviation $\sigma = \sqrt{N_{sig}}$. The interpolated test statistic distributions are given by

$$TS(N_{sig}) = \sum_i TS(N_{sim,i}) \cdot \int_{N_{sim,i}-\Delta_{sim}/2}^{N_{sim,i}+\Delta_{sim}/2} p_{gaus}(N)dN ,$$
(13)

where i runs over all generated test statistics. The result of the pseudo-experiments (number of signal neutrinos) was smeared by a Gaussian with width corresponding to the systematic uncertainties, as described in Sect. 7. Systematic errors, including the uncertainty on the effective area, are thus included in the effective upper limits on the number of events, listed in Table 4. These can be directly translated to limits on $\langle \sigma_A v \rangle$ using Eq. (12).

Table 4 Effective 90 % CL Feldman–Cousins limit on the number of signal events in the data set, N_{UL}, for different halo profiles. The values include systematics and can be directly translated to limits on $\langle \sigma_A v \rangle$ using Eq. (12)

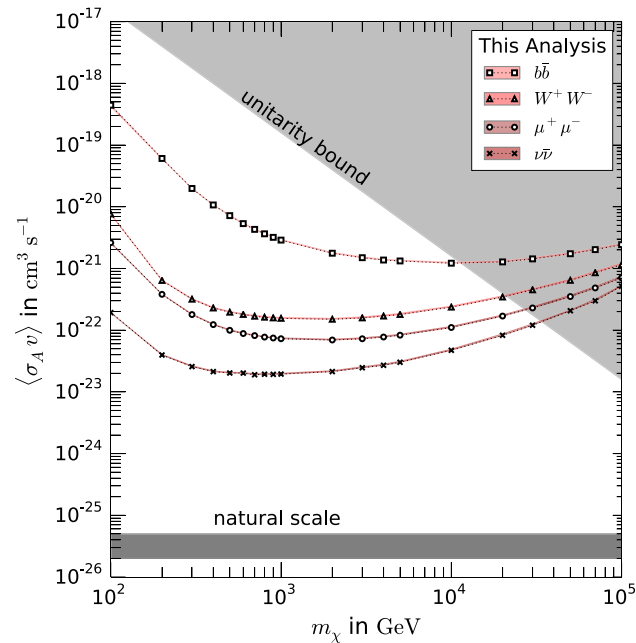| Halo profile	N_{UL}
NFW	949
Burkert	1014

Fig. 16 Exclusion limits on dark matter self-annihilation cross-section from this analysis at 90 % CL. The baseline limit curves are calculated for the NFW profile. The model-dependence has been estimated from the Burkert profile and are shown as *bands*, which are very narrow and thus hard to see. The *gray band* describes the natural scale if all dark matter consists of WIMPs and the *gray upper region* is excluded by the unitarity bound [5]

By using Eq. (12) the limit on the signal events N_{UL} can be interpreted in terms of a limit on the self-annihilation cross-section $\langle \sigma_A v \rangle_{UL}$. The resulting limits are shown in Fig. 16 as function of m_χ and for the different benchmark annihilation channels. The limits are also listed in Table 5. In correspondence to the experimental exclusion limit it is possible to calculate the average upper limit, which gives the mean expected exclusion limit in case of no signal [52]. The average effective upper limit on the number of signal neutrinos in case of an W^+W^- annihilation channel and a dark matter particle mass of 600 GeV is $\langle N_{UL} \rangle = 747$. Note that the average upper limit is more stringent by 10–24 % than the resulting exclusion limits depending on the halo profile annihilation channel and dark matter particle mass.

Table 5 Limit on the self-annihilation cross-section $\langle \sigma_A v \rangle$ for different annihilation channels, halo profiles and DM-particle masses m_χ

m_χ (GeV)	$\langle \sigma_A v \rangle$ (cm^3 s^{-1})			
	$b\bar{b}$	W^+W^-	$\mu^+\mu^-$	$\nu\bar{\nu}$
Assuming Burkert profile				
100	4.2×10^{-19}	7.6×10^{-21}	2.6×10^{-21}	1.9×10^{-22}
200	6.0×10^{-20}	6.5×10^{-22}	3.8×10^{-22}	4.0×10^{-23}
300	2.0×10^{-20}	3.2×10^{-22}	1.8×10^{-22}	2.6×10^{-23}
400	1.1×10^{-20}	2.3×10^{-22}	1.3×10^{-22}	2.2×10^{-23}
500	7.3×10^{-21}	2.0×10^{-22}	1.0×10^{-22}	2.1×10^{-23}
600	5.4×10^{-21}	1.8×10^{-22}	9.0×10^{-23}	2.1×10^{-23}
700	4.4×10^{-21}	1.7×10^{-22}	8.4×10^{-23}	2.0×10^{-23}
800	3.7×10^{-21}	1.7×10^{-22}	7.9×10^{-23}	2.0×10^{-23}
900	3.3×10^{-21}	1.6×10^{-22}	7.7×10^{-23}	2.0×10^{-23}
1,000	2.9×10^{-21}	1.6×10^{-22}	7.5×10^{-23}	2.0×10^{-23}
2,000	1.8×10^{-21}	1.5×10^{-22}	7.1×10^{-23}	2.2×10^{-23}
3,000	1.5×10^{-21}	1.6×10^{-22}	7.5×10^{-23}	2.5×10^{-23}
4,000	1.4×10^{-21}	1.8×10^{-22}	8.0×10^{-23}	2.8×10^{-23}
5,000	1.4×10^{-21}	1.9×10^{-22}	8.6×10^{-23}	3.1×10^{-23}
10,000	1.3×10^{-21}	2.5×10^{-22}	1.1×10^{-22}	4.9×10^{-23}
20,000	1.3×10^{-21}	3.6×10^{-22}	1.8×10^{-22}	8.7×10^{-23}
30,000	1.5×10^{-21}	4.7×10^{-22}	2.4×10^{-22}	1.3×10^{-22}
50,000	1.8×10^{-21}	6.7×10^{-22}	3.7×10^{-22}	2.1×10^{-22}
70,000	2.1×10^{-21}	8.9×10^{-22}	5.1×10^{-22}	3.2×10^{-22}
10,0000	2.5×10^{-21}	1.2×10^{-21}	7.4×10^{-22}	5.3×10^{-22}
Assuming NFW profile				
100	4.4×10^{-19}	7.6×10^{-21}	2.6×10^{-21}	1.9×10^{-22}
200	6.1×10^{-20}	6.4×10^{-22}	3.8×10^{-22}	4.0×10^{-23}
300	2.0×10^{-20}	3.2×10^{-22}	1.8×10^{-22}	2.6×10^{-23}
400	1.1×10^{-20}	2.3×10^{-22}	1.2×10^{-22}	2.1×10^{-23}
500	7.2×10^{-21}	2.0×10^{-22}	1.0×10^{-22}	2.0×10^{-23}
600	5.3×10^{-21}	1.8×10^{-22}	8.8×10^{-23}	2.0×10^{-23}
700	4.3×10^{-21}	1.7×10^{-22}	8.2×10^{-23}	1.9×10^{-23}
800	3.6×10^{-21}	1.6×10^{-22}	7.7×10^{-23}	1.9×10^{-23}
900	3.2×10^{-21}	1.6×10^{-22}	7.5×10^{-23}	1.9×10^{-23}
1,000	2.9×10^{-21}	1.6×10^{-22}	7.3×10^{-23}	1.9×10^{-23}
2,000	1.8×10^{-21}	1.5×10^{-22}	6.9×10^{-23}	2.1×10^{-23}
3,000	1.5×10^{-21}	1.6×10^{-22}	7.3×10^{-23}	2.5×10^{-23}
4,000	1.4×10^{-21}	1.7×10^{-22}	7.7×10^{-23}	2.7×10^{-23}
5,000	1.3×10^{-21}	1.8×10^{-22}	8.3×10^{-23}	3.0×10^{-23}
10,000	1.2×10^{-21}	2.4×10^{-22}	1.1×10^{-22}	4.7×10^{-23}
20,000	1.3×10^{-21}	3.4×10^{-22}	1.7×10^{-22}	8.3×10^{-23}
30,000	1.4×10^{-21}	4.5×10^{-22}	2.3×10^{-22}	1.2×10^{-22}
50,000	1.7×10^{-21}	6.4×10^{-22}	3.5×10^{-22}	2.1×10^{-22}
70,000	2.0×10^{-21}	8.5×10^{-22}	4.8×10^{-22}	3.0×10^{-22}
100,000	2.4×10^{-21}	1.2×10^{-21}	7.1×10^{-22}	5.2×10^{-22}

9 Discussion

Compared to the predecessor analysis of IC22 data using a cut-and-count based method [20], the effective area increases by more than an order of magnitude in the low energy region ($\sim$100 GeV) but just a factor of about 3 at high energies ($\sim$10 TeV) in the relevant zenith region. The larger gain in effective area for low dark matter masses is caused by Deep-Core, the low-energy extension of IceCube, which was not implemented in IC22, but was already in operation in IC79. The lager gain in the effective area at low energies causes an increase in sensitivity of more than an order of magnitude at these energies. However due to a much larger sample size, caused by the large increase in the number of low energy events, and just a slight increase in effective area at high energies, there is just a small gain in sensitivity for high dark matter masses. As this analysis measures an over-fluctuation and the IC22 analysis has measured a under-fluctuation the exclusion limits of the IC22 analysis are more stringent for high dark matter masses of a few TeV. However the limits in the low-mass region of 100 GeV are still an order of magnitude more stringent due to the larger increase in sensitivity. For comparison the exclusion limits (90 % CL) of the

predecessor analysis are shown in Fig. 17. Note that in the predecessor analysis a NFW profile was assumed, but with a local density of 0.3 GeV/cm^3, while here 0.47 GeV/cm^3 is assumed. For reasons of comparison the limits in Fig. 17 have been rescaled to the local density used in this analysis.

Furthermore, exclusion limits of an outer Galactic halo analysis by Fermi-LAT [53] are also shown in Fig. 17 for annihilation into $b\bar{b}$ and $\mu^+\mu^-$. This analysis has measured the γ-ray emission along the Galactic plane in a window of $\pm15°$, whereas the central $\pm5°$ are excluded. In [53] a NFW profile was assumed, but with a local density of 0.43 GeV/cm^3, while here 0.47 GeV/cm^3 is assumed. For reasons of comparison the limits in Fig. 17 have been rescaled to the local density used in this analysis. It can be seen that for hard neutrino channels ($\mu^+\mu^-$) the exclusion limits of this analysis come close to the outer Galactic halo limits of Fermi.

The most stringent exclusion limits from γ-ray telescopes in the energy-range of this analysis are set by HESS [55], with an analysis focusing on the Galactic Center, and Fermi [56] with an analysis focusing at dwarf galaxies. These limits are about two orders of magnitude more stringent. However it is important to note, that the systematic uncertainties for γ-ray and neutrino telescopes are of very different nature. Also γ

Fig. 17 Exclusion limits on dark matter self-annihilation cross-section from outer Galactic halo searches only. The results of this analysis and exclusion limits from the predecessor analysis of IceCube-22 [20] (both 90 % CL) and from the Fermi-LAT [53] (3σ CL) are shown. The baseline limit curves are calculated for the NFW profile, however different normalization parameter are used. For reasons of comparison the limits from IC22 and Fermi are rescaled to the local density of $\rho_{SC} = 0.47$ GeV/cm^3 that is used in this analysis. The *gray band* describes the natural scale if all dark matter consists of WIMPs and the *gray upper region* is excluded by the unitarity bound [5]
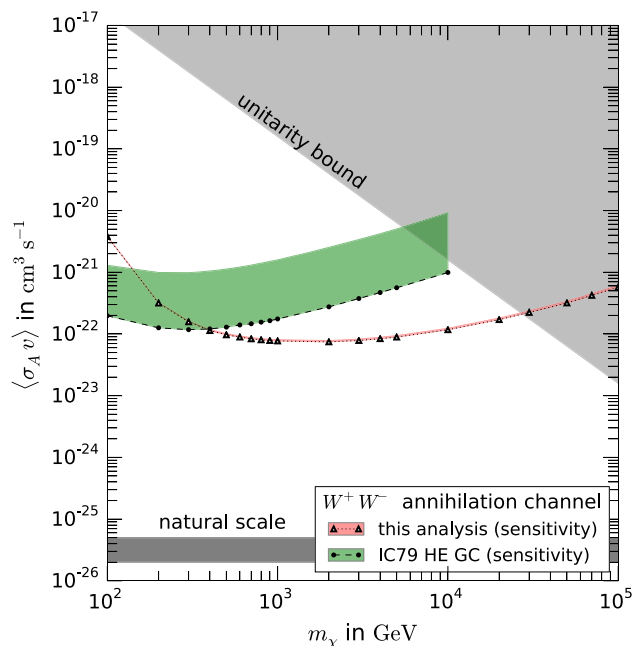
Fig. 18 Median sensitivity on dark matter self-annihilation cross-section assuming annihilation in W^+W^- for this analysis and for the IceCube-79 high energy Galactic Center analysis (IC79 HE GC) [54]. The baseline limit curves are calculated for the NFW profile (*markers*). The model-dependence (*bands*) has been estimated from the Burkert profile. The *gray band* describes the natural scale if all dark matter consists of WIMPs and the *gray upper region* is excluded by the unitarity bound [5]

telescopes have the highest sensitivity for the soft channel and vice versa, smallest sensitivity for the hard channels.

The halo profile dependencies in this analysis are very small compared to the Galactic Center analysis of IceCube. This can be seen by comparing this analysis with a Galactic Center search, that focuses on the central part of the galaxy. The sensitivity for the W^+W^- annihilation channel of the IceCube-79 Galactic Center analysis described in [54] and the sensitivity of this analysis are compared in Fig. 18. The bands represent the model uncertainties determined from Burkert and NFW profile, whereas NFW is used as baseline. It is clearly visible that the halo profile uncertainties are much smaller for a halo analysis (compare Fig. 2), while the overall sensitivity of the two approaches are remarkably similar.

10 Conclusions

We have presented a competitive analysis technique to search for characteristic anisotropies by using a multipole expansion of the neutrino arrival direction sky map. It was found that the multipole analysis is a sensitive and robust analysis method, that has the feature to reduce systematic uncertainties in an easy way.

We applied the analysis to one year of data taken with the IceCube detector in its the nearly completed detector configuration. The search for a neutrino flux, resulting from dark matter annihilation, has found no significant deviation from the background expectation. Exclusion limits on the self-annihilation cross-section $\langle \sigma_A v \rangle$ were calculated approaching 1.9×10^{-23} cm^3 s^{-1}. The resulting exclusion limits are more stringent than the predecessor analysis of IC22 data in a wide parameter range. Furthermore the extracted limits come close to limits from γ-experiments, that also focus on the outer Galactic halo, for hard annihilation channels and large dark matter masses. The presented analysis, focusing on the Galactic halo, is very robust against halo profile uncertainties compared to analyses targeting the Galactic Center or dwarf spheroidal galaxies (compare Fig. 2).

References

1. D. Larson et al., Astrophys. J. Suppl. **192**, 16 (2011)
2. Planck Collaboration, P.A.R. Ade et al.(2013). arXiv:1303.5076
3. G. Bertone, D. Hooper, J. Silk, Phys. Rep. **405**, 279 (2005)
4. G. Steigman, M.S. Turner, Nucl. Phys. B **253**, 375 (1985)
5. K. Griest, M. Kamionkowski, Phys. Rev. Lett. **64**, 615 (1990)
6. M. Lindner, A. Merle, V. Niro, Phys. Rev. D **82**, 123529 (2010)
7. PAMELA Collaboration, O. Adriani et al., Nature **458**, 607 (2009)
8. Fermi-LAT Collaboration, M. Ackermann et al., Phys. Rev. Lett. **108**, 011103 (2012)
9. AMS Collaboration, M. Aguilar et al., Phys. Rev. Lett. **110**, 141102 (2013)
10. AMS Collaboration, L. Accardo et al., Phys. Rev. Lett. **113**, 121101 (2014)
11. I.V. Moskalenko, A.W. Strong, Astrophys. J. **493**, 694 (1998)
12. H. Yuksel, M.D. Kistler, T. Stanev, Phys. Rev. Lett. **103**, 051101 (2009)
13. P. Meade, M. Papucci, A. Strumia, T. Volansky, Nucl. Phys. B **831**, 178 (2010)
14. M. Cirelli, M. Kadastik, M. Raidal, A. Strumia, Nucl. Phys. B **813**, 1 (2009)
15. IceCube Collaboration, R. Abbasi et al., Phys. Rev. D **85**, 042002 (2012)
16. AMANDA Collaboration, J. Ahrens et al., Phys. Rev. D **66**, 032006 (2002)
17. IceCube Collaboration, R. Abbasi et al.(2012). arXiv:1210.3557
18. IceCube Collaboration, M. Aartsen et al., Search for dark matter annihillation in the galactic center with IceCube-79 (2015) (in preparation)
19. IceCube Collaboration, M.G. Aartsen et al., Phys. Rev. D **88**, 122001 (2013)
20. IceCube Collaboration, R. Abbasi et al., Phys. Rev. D **84**, 022004 (2011)
21. Milagro Collaboration, A. Abdo et al., Astrophys. J. **698**, 2121 (2009)
22. L.G. Sveshnikova, O.N. Strelnikova, V.S. Ptuskin, Astropart. Phys. **50**, 33 (2013)
23. IceCube Collaboration, R. Abbasi et al., Astrophys. J. Lett. **718**, L194 (2010)
24. ARGO-YBJ Collaboration, B. Bartoli et al., Phys. Rev. D **88**, 082001 (2013)
25. IceCube Collaboration, A. Achterberg et al., Astropart. Phys. **26**, 155 (2006)
26. IceCube Collaboration, R. Abbasi et al., Astropart. Phys. **35**, 615 (2012)
27. IceCube Collaboration, R. Abbasi et al., Nucl. Instrum. Methods A **601**, 294 (2009)
28. J. Diemand, M. Kuhlen, P. Madau, Astrophys. J. **667**, 859 (2007)

29. J. Diemand et al., Nature **454**, 735 (2008)
30. V. Springel et al., Mon. Not. R. Astron. Soc. **391**, 1685 (2008)
31. L. Hernquist, Astrophys. J. **356**, 359 (1990)
32. J.F. Navarro, C.S. Frenk, S.D.M. White, Astrophys. J. **462**, 563 (1996)
33. J.F. Navarro, C.S. Frenk, S.D.M. White, Astrophys. J. **490**, 493 (1997)
34. F. Nesti, P. Salucci, J. Cosmol. Astropart. Phys. **1307**, 016 (2013)
35. A. Burkert, Astrophys. J. Lett. **447**, 25 (1995)
36. H. Yuksel, S. Horiuchi, J.F. Beacom, S. Ando, Phys. Rev. D **76**, 123506 (2007)
37. P. Gondolo, J. Cosmol. Astropart. Phys. **0407**, 008 (2004)
38. Particle Data Group (PDG), J. Beringer et al., Phys. Rev. D **86**, 010001 (2012)
39. S.S. Keerthi, S.K. Shevade, C. Bhattacharyya, K.R.K. Murthy, Neural Comput. **13**, 637 (2001)
40. IceCube Collaboration, M.G. Aartsen et al., The IceCube Neutrino Observatory Part I: Point Source Searches, 2013. *Proceedings of 33rd International Cosmic Ray Conference (ICRC)*. arXiv:1309.6979
41. IceCube Collaboration, M. Aartsen et al., Astrophys. J. **779**, 132 (2013)
42. J.D. Jackson, *Classical Electrodynamics*, 3rd edn. (Wiley, New York, 1998)
43. http://healpix.jpl.nasa.gov. Accessed 26 June 2014
44. K.M. Górski et al., Astrophys. J. **622**, 759 (2005)
45. R. Reimann, Suche nach Neutrinos aus der Annihilation dunkler Materie im Galaktischen Halo mit IceCube. Master's thesis, III. Physikalisches Institut B, RWTH Aachen University (2013)
46. M. Leuermann, Search for diffuse neutrino point sources using a multipole analysis in IceCube. Master's thesis, III. Physikalisches Institut B, RWTH Aachen University (2013)
47. IceCube Collaboration, M. Aartsen et al.(2014). arXiv:1408.0634
48. M. Kamionkowski, S.M. Koushiappas, M. Kuhlen, Phys. Rev. D **81**, 043532 (2010)
49. IceCube Collaboration, R. Abbasi et al., Nucl. Instrum. Methods A **618**, 139 (2010)
50. IceCube Collaboration, M.G. Aartsen et al., Nucl. Instrum. Methods A **711**, 73 (2013)
51. G.J. Feldman, R.D. Cousins, Phys. Rev. D **57**, 3873 (1998)
52. G.C. Hill, K. Rawlins, Astropart. Phys. **19**, 393 (2003)
53. Fermi-LAT Collaboration, M. Ackermann et al., Astrophys. J. **761**, 91 (2012)
54. IceCube Collaboration, M. Aartsen et al., The IceCube Neutrino Observatory Part IV: Searches for Dark Matter and Exotic Particles, 2013. *Proceedings of 33rd International Cosmic Ray Conference (ICRC)*. arXiv:1309.7007
55. H.E.S.S. Collaboration, A. Abramowski et al., Phys. Rev. Lett. **106**, 161301 (2011)
56. Fermi-LAT Collaboration, M. Ackermann et al., Phys. Rev. Lett. **107**, 241302 (2011)